Enabling simulations of grains within a full rotation range in amplitude expansion of the phase-field crystal model

Matjaž Berčič* and Goran Kugler†
University of Ljubljana, Faculty of Natural Sciences and Engineering, Department of Materials and Metallurgy
(Dated: 27 April 2020)

This paper introduces improvements to the amplitude expansion of the phase field crystal model (APFC) that enable the simulation of grains within a full range of orientations. The unphysical grain boundary between grains, rotated by a crystal's symmetry rotation, is removed using a combination of the auxiliary rotation field described in our previous work and an algorithm that correctly matches the complex amplitudes according to the differences in local rotation.
Published in Physical Review E DOI 10.1103/PhysRevE.101.043309

I. INTRODUCTION

The microstructure plays a crucial role in determining the properties of many modern industrially important materials. Since experiments are expensive and the relationships between chemical composition, thermo mechanical processing, and the final microstructure are complex, computer simulations are an important step in the design of new materials. In order to be able to competitively price the final product, material production usually occurs in large batches of material. Computer simulations able to efficiently model processes occurring on such a large span of spatial and temporal scales are scarce, and frequently include a hierarchy of different models for modeling processes on different scales that exchange parameters. Discontinuous transitions between the different scales sometimes introduce nonphysical phenomena that are hard to eliminate, therefore making use of a single model preferable. In order to enable modeling of the microstructure on diffusive time scales, the phase-field-crystal model (PFC) was developed [1, 2]. A recently developed amplitude expansion of the PFC model (APFC) [3, 4] can predict the microstructure of materials in relatively large simulation domains, and in combination with effective mesh refinement techniques (AMR) [5, 6] can span many different scales in a continuous manner.

The PFC and APFC models were successfully applied to the study of many different phenomena such as ferromagnetic [7] and ferroelectric [8] effects, the effects of hydrodynamic velocity on the microstructure formation [9], the study of grain boundary motion and polycrystalline films [3, 4, 10], structural phase transitions [11–13] and grain boundary energies [14, 15]. The models were improved to cover a wide range of possible materials, including materials with different crystal lattices [13, 14, 16–21] in 2D and 3D, materials with spatial anisotropy [22], liquid crystals [23, 24], binary systems [20, 25, 26] and multi-component alloys [27], improved to achieve instantaneous mechanical equilibrium [28] and tune the energy of defects and interfaces [15].

In our recent work [6], we presented a new way to achieve adaptive mesh refinement in APFC models using an auxiliary local rotation field. The local rotation field was derived from the fields used in the computation, but was itself never used in calculations. It was used only to convert the amplitude equations in a system, aligned with the local grain, where the so-called beats in the amplitudes disappeared and AMR algorithm was able to coarsen the mesh.

In this work we show how the local rotation field can be used to eliminate an unphysical grain boundary described by Spatschek *et al.* [26], occurring between grains rotated by a crystal's symmetry rotation, and enable APFC simulations with a whole range of grain orientations. This can enable APFC simulations of industrially important thermo-mechanical processes where grain rotation occurs, such as the hot and cold forming of metallic materials.

II. APFC MODEL

The PFC model operates on a local atomic density function ψ which minimizes the free energy functional [1, 2, 14, 28] given here in terms of dimensionless field ψ tracking the deviations of the atomic density field from its average

$$F = \int d\mathbf{r} \left\{ \frac{\Delta B}{2}\psi^2 + B^x \frac{\psi}{2}(1+\nabla^2)^2\psi - \frac{t}{3}\psi^3 + \frac{v}{4}\psi^4 \right\} \tag{1}$$

where $\Delta B = B^l - B^x$. Parameter B^l is related to the compressibility of the liquid state and B^x to the elastic moduli of the crystalline state. The choice of t and v determines the magnitude of the amplitudes and the liquid-solid miscibility gap. The single-mode solution of the PFC equation in the solid phase has honeycomb symmetry within a certain range of parameters and the solution can be approximated as [3–5]

$$\psi \approx \sum_{j=1}^{3} A_j e^{i\mathbf{k_j}\cdot\mathbf{x}} + \sum_{j=1}^{3} A_j^* e^{-i\mathbf{k_j}\cdot\mathbf{x}} \tag{2}$$

* corresponding author: matjaz.bercic@omm.ntf.uni-lj.si
† goran.kugler@omm.ntf.uni-lj.si

where A_j are the complex amplitudes of waves aligned with the wave vectors

$$\begin{aligned}\mathbf{k}_1 =& k_0(-\vec{i}\sqrt{3}/2 - \vec{j}/2),\\ \mathbf{k}_2 =& \quad k_0\vec{j},\\ \mathbf{k}_3 =& \; k_0(\vec{i}\sqrt{3}/2 - \vec{j}/2),\end{aligned} \tag{3}$$

In order to be able to compare our results with already published results, we used the same free energy functional and dynamic equations for our APFC model as in Hirvonen *et al.* [14]. The free energy and the dynamic equations are

$$\begin{aligned}F =& c_A \int d\mathbf{r}\{(\Delta B/2)A^2 + (3v/4)A^4 - 2t(\textstyle\prod_{j=1}^{3} A_j + c.c.)\\ &+ \textstyle\sum_{j=1}^{3}(B^x|\mathcal{L}_j A_j|^2 - (3v/2)|A_j|^4)\}\end{aligned} \tag{4}$$

$$\frac{\partial A_j}{\partial t} = -[\Delta B + B^x\mathcal{L}_j^2 + 3v(A^2 - |A_j|^2)]A_j + 2t\prod_{k\neq j} A_k^* \tag{5}$$

where $\mathcal{L}_j = \nabla^2 + 2\mathbf{k}_j\cdot\nabla$ and $A^2 = 2\sum_{j=1}^{3}|A_j|^2$. The dynamic equations are derived using non-conserved, dissipative dynamics. We chose the same set of parameters as Hirvonen *et al.* [14] ($B^l = 1$, $B^x = 0.98$, $t = -1/2$, $v = 1/3$, $c_A = 7.95eV$, $a_0 = 2.46$Å).

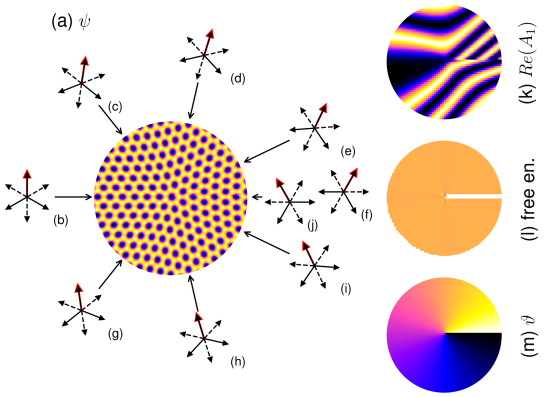

FIG. 1. The figure presents (a) atomic density around a wedge defect, (b)-(j) base vectors rotated to match the rotation of the local lattice expressed through the beats in the complex amplitudes (k), (l) free energy density and (m) rotation of the base vectors. Because a wedge defect breaks the rotational symmetry of the crystal, encircling it once will shift the directions in which the basis vectors point by one symmetry rotation of the crystal lattice. As the APFC model can't connect the rotation expressed through the beats with the rotation of the base vectors, an unphysical grain boundary occurs as seen in (l).

III. LIMITATIONS OF THE APFC MODEL

The amplitude expansion of the PFC model approximates the solution for the atomic density function ψ with a sum of atomic density waves aligned with the first 3 vectors of the reciprocal lattice as described in eq. (2). A complex amplitude A_j describes density variation in direction corresponding to its wave vector. In case the grain is rotated relative to the initially chosen set of base vectors, the rotation is expressed through the beats in the complex amplitudes $A_j^{'} = A_j^0 e^{i(\mathbf{k}_j(\vartheta) - \mathbf{k}_j)\cdot\mathbf{x}}$ where A_j^0 and $\mathbf{k}_j(\vartheta)$ are the complex amplitudes and base vectors in a system, aligned with the rotated grain.

The real rotation of the grains is therefore determined by two disconnected parts of the model, the beats in the complex amplitudes which express the rotation of the grain relative to the initially chosen base vectors, and the rotation of the initially chosen set of base vectors. The unphysical grain boundary in the APFC model appears due to the model's inability to connect both expressions of grain rotation.

A grain with complex amplitudes (A_1, A_2, A_3), rotated by 60°, can be represented by beats in the complex amplitudes corresponding to 60° rotation. As a 60° rotation of the crystal lattice, in a system with 60° rotational symmetry, corresponds to a re-assignment of complex amplitudes to base vectors, it could also be represented by the amplitudes (A_2^*, A_3^*, A_1^*) with no beats. Since the APFC model can't connect both representations for physically the same grain, an unphysical grain boundary [26] with characteristics of a 60° grain boundary forms in the model where both representations meet.

This phenomena prevents the application of the APFC model to the study of processes where grain rotation occurs, or grain rotation can not be feasibly limited to less than half of the crystal's symmetry rotation. The limit on grain rotations is enforced in most published studies [5, 14, 15, 29], which either study only grain boundaries at lower angles, or resort to using a different simulation setup for grain boundaries with mismatch angles above half of the crystal symmetry rotation.

To highlight this limitation of the APFC model and its consequences, we calculated the complex amplitudes A_j around the core of a wedge defect where the rotational symmetry of the crystal lattice is broken. The chosen wedge defect exhibits a 7-fold rotational symmetry in its core as shown in the center of Fig. 1(a), whereas the normal lattice has 6-fold rotational symmetry. The initial condition that yields this wedge dislocation is obtained by $\vartheta(x,y) = 0 - (2\pi + atan2(y,x) \textbf{ mod } 2\pi)/6 + \pi/6$, $A_j^{'} = A_j^0 e^{i(\mathbf{k}_j(\vartheta(x,y)) - \mathbf{k}_j)\cdot\mathbf{x}}$. Due to the nature of the wedge defect, encircling it one time will yield a 60° rotation of the lattice vectors (one symmetry rotation of the crystal lattice) and show an unphysical grain boundary in the APFC model due to the mentioned limitations of the model. Since pairs of wedge disclinations appear on the grain boundaries in graphene frequently studied with the APFC model [15], and pairs of complementary disclinations are equivalent to dislocations [30], the example also highlights a detail that occurs in many APFC

simulations.

Figure 1(a) shows the atomic density function around a wedge defect in the center of the image. Highlights (b)-(j) show the local orientation of the base vectors at different points around the wedge defect. The misalignment of the local lattice with the initial choice of base vectors is expressed through the beats in the complex amplitudes presented in (k). Encircling the wedge defect from above (b)-(f) rotates the atomic lattice by 30° clockwise. Encircling the same defect core from below (b),(g)-(j) rotates the atomic lattice by 30° counter-clockwise. This means that the rotation expressed by the beats differs by 60° on the line where both expressions of the rotation meet (marked with (j) and (f)), therefore creating an unphysical grain boundary in the APFC model. Figure 1 (k) shows real part of the first complex amplitude $Re(A_0)$. The frequency of the beats gradually increases when encircling the defect core from either side, but as the rotation of the lattice expressed through the beats is different, in the area marked with (j) and (f) where both rotations meet, the beats on both sides do not match, and an unphysical grain boundary is formed, as also presented in a free energy plot in Fig. 1 (l). Figure 1 (m) shows the rotation of the atomic lattice that is expressed through the beats ranging from $-30°$ to $+30°$.

IV. DESCRIPTION OF IMPROVEMENTS TO THE MODEL

Our model introduces a set of locally-rotated complex amplitudes [6] A_j^ϑ

$$A_j = A_j^\vartheta e^{i\delta\mathbf{k}_j(\vartheta)\cdot\mathbf{x}} \tag{6}$$

where ϑ is a local rotation field and $\mathbf{k}_j(\vartheta) = \mathbf{k}_j + \delta\mathbf{k}_j(\vartheta)$ are rotated basis vectors. The local rotation field ϑ is incrementally derived from the complex amplitudes A_j based on the observation that, when the rotation of the basis vectors matches the rotation of the local grain, the beats disappear and therefore the gradient of the locally rotated amplitudes is zero:

$$\nabla A_j^\vartheta = (\nabla A_j)e^{-i\delta\mathbf{k}_j\cdot\mathbf{x}} + A_j(-i\delta\mathbf{k}_j)e^{-i\delta\mathbf{k}_j\cdot\mathbf{x}} = 0 \tag{7}$$

We incrementally update the local rotation field using

$$\delta\mathbf{k}_j(\vartheta) = \frac{\nabla A_j}{iA_j} = \mathbf{k}_j(\vartheta) - \mathbf{k}_j \tag{8}$$

where we average the rotation angle derived from (8) over all complex amplitudes. Due to the rotational covariance of the operator $\mathcal{L}_j$, the conversion between the basis vectors rotated by a different amount can be separated from the operator evaluation, and the adaptive mesh can coarsen in all grains, regardless of the orientation. The use of local rotation adds no additional error to the calculations (see Appendix A). To apply an operator $\mathcal{L}_j$ on a locally rotated field $X \in \{A_j^\vartheta, L_j^\vartheta A_j^\vartheta\}$, the local rotation is treated separately as in [6]

$$\mathcal{L}_j^\vartheta X_j^\vartheta = e^{-i\delta\mathbf{k_j}\cdot\mathbf{x}}\mathcal{L}_j X_j \tag{9}$$

In the current work, we present a new way to eliminate the unphysical grain boundary between grains rotated by a crystal's symmetry rotation, using a local rotation field in combination with an algorithm that uses the local rotation field to correctly match the complex amplitudes corresponding to base vectors pointing in most similar directions in the entire simulation domain. The unphysical grain boundary in the APFC model occurs because the model can not connect the rotation of the base vectors for the amplitudes with the rotation expressed through the beats of the complex amplitudes. To solve this problem, our algorithm correctly matches the complex amplitudes based on the total rotation, expressed through both beats and the rotation of base vectors.

Numerical implementation of the algorithm uses a lookup table to match the correct complex amplitudes. We calculate a local rotation field that tracks the rotation expressed through the beats in the complex amplitudes as in [6]. When operating with values from different computational nodes in the same calculation, we correct the values for the differences in the local rotation as in [6], and if the difference in the local rotation exceeds half of the crystal's symmetry rotation, we match the amplitudes that correspond to the most similar physical directions. In effect this means that when the neighboring computation nodes differ in rotation by 60°, we use A_2^* of the second node instead of A_1 when calculating the values of operators in the first computation node. The approximation of the single-mode solution (2) is the sum of planar waves directed at angles that are multiples of the crystal's symmetry rotation. Table I lists the wave vectors, the angles they form with the first wave vector $\mathbf{k}_1$, the complex amplitudes A_j matching the selected wave vector, and the wave vectors we obtain with one crystal's symmetry rotation ($\pm 60°$). Our algorithm finds the best matching complex amplitudes in neighboring computational nodes by comparing the local rotation of both nodes. If the local rotation ϑ differs by more than half of the crystal's symmetry rotation ($|\vartheta_L - \vartheta_R| > 30°$), the algorithm matches the complex amplitude A_1 in one

TABLE I. A list of wave vectors, their rotation and corresponding amplitudes. The matching amplitudes when the rotation is shifted by one crystal's symmetry rotation in either direction are shown in the table's last two columns.

Direction	Rotation	Amp.	Amp. $(+60°)$	Amp. $(-60°)$
$+\mathbf{k}_1$	0	A_1	A_2^*	A_3^*
$-\mathbf{k}_2$	60	A_2^*	A_3	A_1
$+\mathbf{k}_3$	120	A_3	A_1^*	A_2^*
$-\mathbf{k}_1$	180	A_1^*	A_2	A_3
$+\mathbf{k}_2$	240	A_2	A_3^*	A_1^*
$-\mathbf{k}_3$	300	A_3^*	A_1	A_2

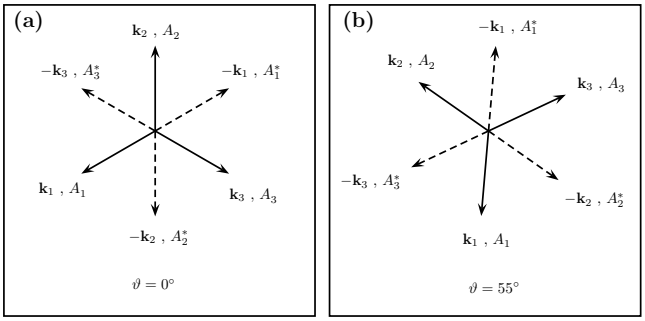

FIG. 2. Wave vectors in two neighboring computational nodes with different local rotations ((a) $\vartheta = 0°$, (b) $\vartheta = 55°$). Our algorithm matches the complex amplitudes that correspond to the wave vectors that point in the closest directions. A_2 in the left computational node (a) is therefore matched with the complex amplitude A_1^* in the right computational node (b), as the angle between the corresponding wave vectors is only 5°.

computational node with A_2^* or A_3^* in the other computational node, depending on the sign of the difference. A full list of matching amplitudes is presented in Table I. In Fig. 2, the wave vectors in two neighboring computational nodes with different local rotations are shown. The algorithm used is the same as in [6], with the following two additions. First, when an operator is evaluated on a locally rotated field, the matching amplitudes from neighboring nodes are used. In case the differences in local rotations between nodes are greater than half of the crystal's symmetry rotation, the matching algorithm uses Table I to find appropriate matching amplitudes. Second, after the optimal local rotation is found in all regions where $|A_j^\vartheta| > A_{\text{min amp.}}$ for all j, the calculated local rotation is copied from each computation node where it is set to all its neighbors where the local rotation is still unset. This process of propagating the local rotation is repeated 10 times.

The first improvement eliminates the unphysical grain boundary occurring between grains that differ in orientations by more than half of the crystal's symmetry rotation. The second improvement is required as the lattice rotation is physically undefined in liquid regions, which initially fill the whole computational domain, and is there set to zero by default. Without the second improvement, the incremental updates to the local rotation start from zero and result in a continuous transition of local rotation across grain boundaries, regardless of the misorientation between grains, which prevents the first improvement from finding the correct matching amplitudes on the interface. Propagating the calculated local rotation into regions where it is yet undefined provides good starting points for the algorithm and enables convergence to correct values even where the correct values change discontinuously at the grain boundary.

The presented improvements to the APFC model change the calculations only in areas where the APFC model gives incorrect results due to the unphysical grain boundary problem described in chapter III. Correct matching of the complex amplitudes introduced by the presented algorithm limits the effective rotations of the atomic lattice to one lattice symmetry rotation with correct periodicity, matching the physical description of the crystal. The improvement therefore only removes existing errors in the model and has no effect on the calculations in the vast majority of the computational domain, where the APFC model is known to work correctly. The origin of the unphysical grain boundary problem might also be seen as a problem with incorrect period of the parameter describing atomic lattice rotation. In the APFC model the lattice rotation is taken as a parameter with values in interval $[0, 2\pi)$, and the unphysical grain boundary occurs as the lattice rotation is physically really a value on a much smaller interval $[0, \vartheta_{\text{symmetry rotation}})$, with periodicity in both intervals. Complex amplitude matching based on the real, physical rotation of the atomic lattice introduced in the presented improvements changes the effective lattice rotations to the interval and periodicity that match the physical properties of the crystal lattice.

V. RESULTS

Figure 3 shows a grain boundary at a 50.1° tilt angle. Without amplitude matching, the result is a grain boundary that would correspond to an effective tilt angle of 50.1°, which is impossible as the crystal's symmetry rotation of 60° limits the effective tilt angles to 30°. With the amplitude matching algorithm, the amplitudes on both sides of the grain boundary that correspond to wave vectors pointing in the most similar directions are properly matched and the result is a grain boundary with a similar structure to a $10° = 60° - 50°$ grain boundary, as expected.

We calculated the grain boundary energies with our improved algorithm and compared them with results published by Hirvonen *et al.* [14]. Our improvements result in the removal of the unphysical effects from improper matching of complex amplitudes on different sides of the grain boundary. In Fig. 4, we show the calculated grain boundary energies in comparison to [14]. In our calculations, we used two different ways of constructing a grain boundary, like [14] we constructed a grain boundary in armchair configuration using two grains that form a vertically oriented grain boundary and used a horizontal grain boundary for the zigzag configuration. The results of calculations obtained without the amplitude-matching algorithm agree well with previous results, and the small differences can be explained by numerical errors introduced by the use of the adaptive mesh refinement techniques and differences in construction of the grain boundaries. Larger differences occur only at tilt angles outside of the range in which a specific grain boundary construction is applicable (above 30° for AC configuration and

Algorithm 1 Local rotation adjustment. Parameters p, q, $A_{\text{min. amp.}}$ and $\vartheta_{\text{max. phase}}$ are heuristic.

for each computation node **do**
  Find optimal rotation ϑ_{opt}:
  if $|A_j^{\vartheta}| > A_{\text{min amp.}}$ for all j **then**
    In solidified regions: from gradient
    for all $j \in \{1,2,3\}$ **do**
      $\delta\mathbf{k}_j(\vartheta_{\text{current}}) = Re\left(\frac{\nabla A_j^{\vartheta_{\text{current}}}}{iA_j^{\vartheta_{\text{current}}}}\right)$
      $\vartheta_{x,j} = 1 + \mathbf{k}_j(\vartheta_{\text{current}}) \cdot \delta\mathbf{k}_j$
      $\vartheta_{y,j} = (\mathbf{k}_j(\vartheta_{\text{current}}) \times \delta\mathbf{k}_j) \cdot \hat{\mathbf{e}}_z$
    end for
    $\vartheta_{\text{opt}} = \vartheta_{\text{current}} + atan2(\sum_j \vartheta_{y,j}/3, \sum_j \vartheta_{x,j}/3)$
  else
    In liquid regions: drop towards zero
    $\vartheta_{\text{opt}} = 0$
  end if
  Smooth the changes
  $\vartheta_{\text{new}} = p \times \vartheta_{\text{current}} + q \times \vartheta_{\text{opt}}$
  Prevent skipping beats
  $d\vartheta = \max_{\{\text{all neighbours NN}\}} |\vartheta_{NN} - \vartheta_{\text{new}}|$ modulo $60°$
  $k_\vartheta = dx\ d\vartheta/\vartheta_{\text{max. phase}}$
  if $k_\vartheta > 1$ **then**
    $\vartheta_{\text{new}} = \vartheta_{\text{current}} + (\vartheta_{\text{new}} - \vartheta_{\text{current}})/k_\vartheta$
  end if
  $\vartheta_{\text{current}} = \vartheta_{\text{new}}$
end for
for $10\times$ propagate local rotation into liquid regions **do**
  for each computation node **do**
    if $|A_j^{\vartheta}| > A_{\text{min. amp.}}$ **then**
      mark node as "rotation is set"
    else if this node has a marked NN **then**
      $\vartheta_{\text{current}}$ = average ϑ over all marked NN
      mark node as "rotation is set"
    end if
  end for
end for

below 30° for ZZ configuration) and in both cases using a local rotation scheme in combination with AMR techniques reduces the error. Results obtained with our amplitude-matching algorithm show a continuous transition between the results obtained with APFC(AC) and APFC(ZZ) configurations at an appropriate angle, confirming the successful removal of the unphysical effects on the grain boundaries.

The grain boundaries were constructed by seeding the simulation domain with a crystal phase upon two opposite rotations, as seen in Fig. 5. The rotation was chosen in such a way that the atomic density on the line between the domains with different orientations is exactly periodical. Before the start of the simulations, we melted the crystal phase in a small area around the grain boundary line. To calculate the grain boundary energy, we averaged the free energy density in the marked area in Fig. 5. The area matches the period of the initial atomic density in y direction and extends into pure, undeformed crystal in x direction. We used sufficiently large simulation domains ($L = 512\pi/2$) to ensure that the center-most area remains periodic in the direction along the grain boundary and the crystal is undeformed at both ends of the marked area. The adaptive mesh refined by 4 levels to $\Delta x = \pi/2 \times 2^4 \approx 25.13$ in the bulk lattice, indicating that the bulk lattice was undeformed in the simulations. Due to these properties of the area over which we averaged the free energy density, the grain boundary energy can be calculated as

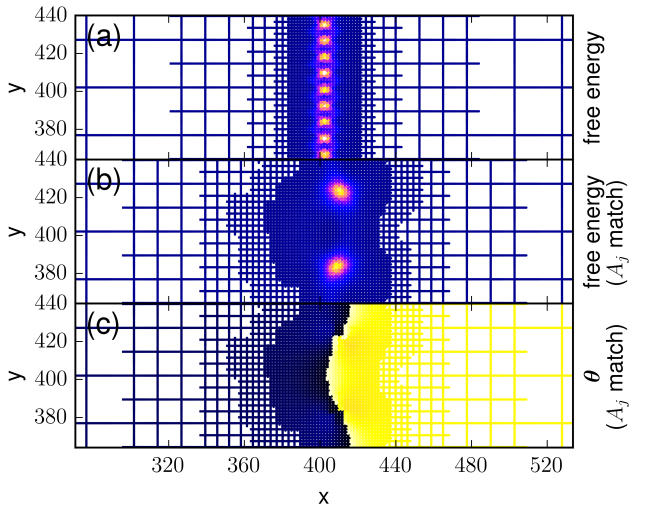

FIG. 3. Free energy on the grain boundary in armchair configuration at a mismatch angle of 50.1°. The top row: (a) shows an unphysical grain boundary that is formed between grains at mismatch angles larger than half of the crystal's symmetry rotation [26]. Middle row: (b) shows the same grain boundary as formed in simulations with our improved algorithm that correctly matches complex amplitudes at different rotations, and therefore the unphysical effects do not occur. Bottom row: (c) shows the local rotation as used in our improved algorithm.

$$\gamma = \Delta F/\Delta y \tag{10}$$

where $\Delta F = F_{\square} - F_{crystal,\square}$ is the increase in free energy in the marked area and Δy is the grain boundary length (in the horizontal grain boundary configuration the axes are switched appropriately).

The effects of our improvements in an example of a simulation with many grains are presented in Fig. 6. 12 seeds with rotations in a full rotation range ($\theta \in [-30°, +30°)$) were grown in undercooled melt using the algorithm presented in this article and compared to our previous work [6]. We can see that the improvements remove unphysically high grain boundary energies on the grain boundaries where the impinging grains are at a tilt angle above 30°. Presuming a completely uniform distribution of grain orientations, this results in the removal of the unphysical effects on half of the grain boundaries.

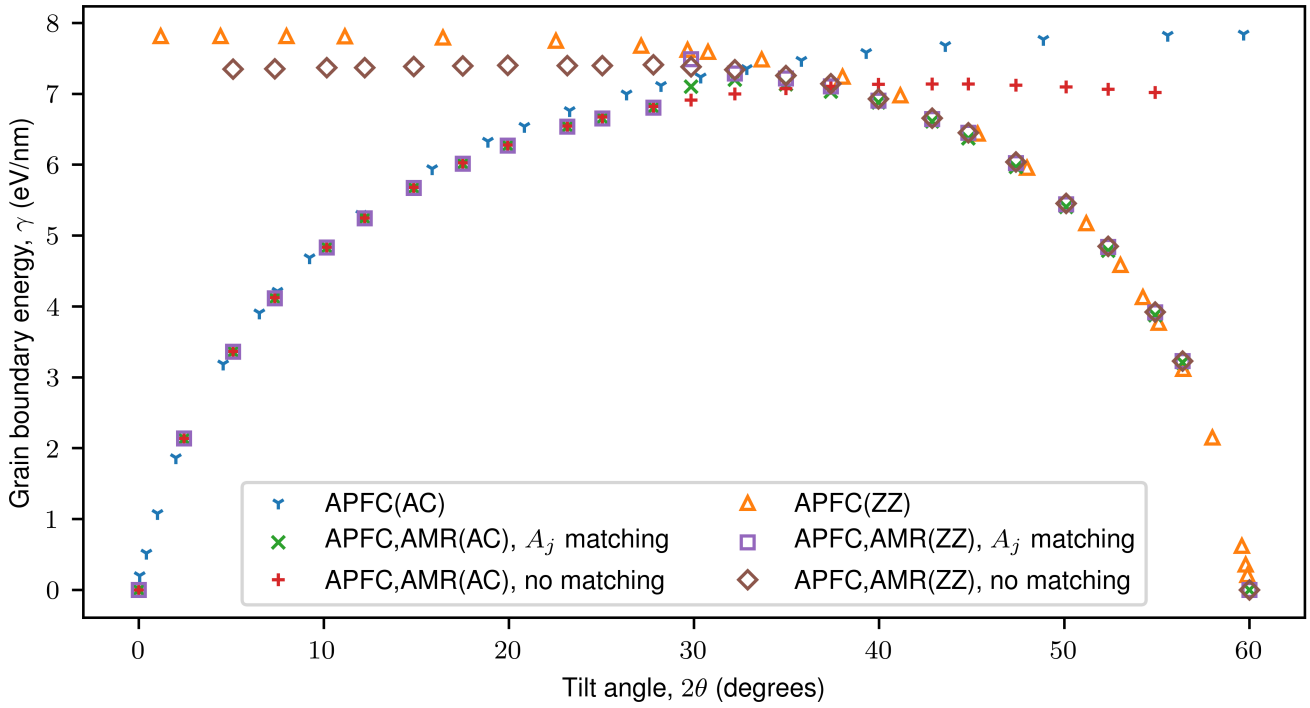

FIG. 4. The grain boundary energy as a function of tilt angle. Values for models APFC(AC) and APFC(ZZ) were published by Hirvonen *et al.* [14] and are in good agreement with our model. Our model without amplitude matching in armchair (AC) and zigzag (ZZ) configurations matches previously published results. Amplitude matching in either configuration successfully removes the unphysical increase in grain boundary energy observed when the tilt angle is more than half of the crystal's symmetry rotation away from a configuration in which complex amplitudes from both impinging grains are completely aligned.

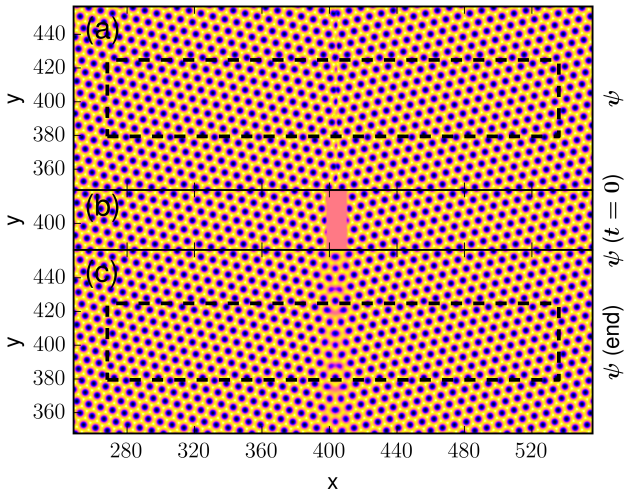

FIG. 5. Grain boundary construction and calculation of free energy. In order to calculate the free energy of a symmetric tilt grain boundary, we simulate two impinging grains, each rotated by an angle at which the microstructure in the middle of the grains repeats periodically, presuming an infinite simulation domain. We calculate the free energy per grain boundary length from the average free energy in the marked regions.

VI. CONCLUSIONS

The presented work introduces a new improvement to the APFC model that removes the unphysical grain boundary, which occurs in the model between grains, rotated by a crystal's symmetry rotation. Presented improvement enables APFC simulations of industrially important processes where grains rotate or grain rotation can not be feasibly limited.

Rotation of grains expressed through the beats in the complex amplitudes is connected with the rotation of the base vectors through an auxiliary local rotation field [6] and a lookup table connecting local rotation to rotation of base vectors for the amplitudes. Grain boundary energies calculated with the improved algorithm match previously published results in correct ranges of values. The improved algorithm enables calculations of grain boundary energies in the entire range of misfits using a single simulation setup where previous approaches required separate simulation setups for armchair and zigzag grain boundary configurations.

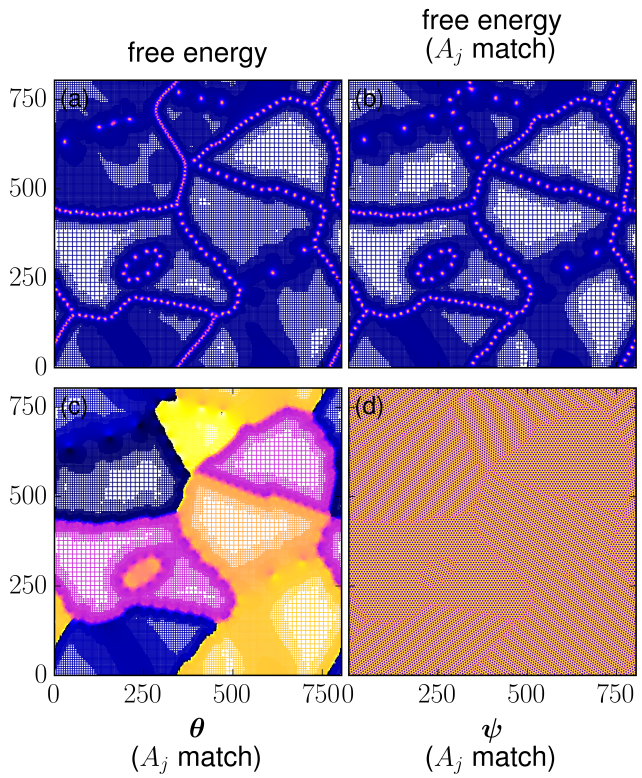

FIG. 6. Grain boundary energies in an example simulation. 12 seeds with rotations in a full rotation range ($\theta \in (-30°, +30°)$) were placed in undercooled melt. The images in the top row show free energy density in the full simulation domain, as calculated: (a) with the algorithm published in [6], and (b) the algorithm presented here. We can see that our improved algorithm removes the unphysical effects on grain boundaries. The images in the bottom row show: (c) the local rotation field; and (d) the reconstructed microstructure.

VII. ACKNOWLEDGMENTS

The authors thank Michael Greenwood for sharing his implementation of an AMR solver described in [31, 32], from which we developed our code. The authors acknowledge financial support from Javna Agencija za Raziskovalno Dejavnost RS (Research Core Funding No. 1000-17-0510 and P2-0344).

Appendix A: Equivalence of APFC calculations in rotated and non-rotated systems

Rotational covariance of the free energy in the APFC model requires that the dynamic equations of the model and free energy density do not depend on the rotation of the initially chosen base vectors.

The conversion of complex amplitudes A_j between systems with differently rotated base vectors $\mathbf{k}_j$ is a multiplication with rotation conversion factor $e^{-i\delta\mathbf{k}_j \cdot x}$ as written in equation (6) [5]. The following appendix provides a proof that the same conversion also holds for all rotationally covariant fields. As a consequence, the calculations performed in systems with different rotations of base vectors can be combined with no additional error. Free energy density, elastic energy and all measurable fields do not change when using local rotation in the calculations.

1. Definitions

$$\Box^{\vartheta} = \{\nabla^2 + 2i\mathbf{k}_j(\vartheta)\cdot\nabla\} \tag{A1}$$

$$\Box = \Box^{\vartheta=0} \tag{A2}$$

$$\mathbf{k}_j(\vartheta) = \mathbf{k}_j + \delta\mathbf{k}_j \tag{A3}$$

$\mathbf{k}_j(\vartheta)$ is $\mathbf{k}_j$ rotated by ϑ, for all $j \in \{1, 2, 3\}$, using cyclical indexes in text.

X is a field expressed in a system with non-rotated base vectors $\mathbf{k}_j$, and X^{ϑ} the corresponding field in system with rotated base vectors $\mathbf{k}_j(\vartheta)$.

$\left[\frac{\partial A_j}{\partial t}\right]$ is the time derivative of the complex amplitude A_j and $\left[\frac{\partial A_j}{\partial t}\right]^{\vartheta}$ is the corresponding time derivative expressed in rotated system.

In general: a symbol without superscript$^{\vartheta}$ marks the same field in non-rotated system.

2. Proof

Lemma 1.1. *From*

$$X^{\vartheta}(\mathbf{x}) = e^{-i\delta\mathbf{k}_j\cdot\mathbf{x}}X(\mathbf{x}) \tag{A4}$$

it follows

$$\Box^{\vartheta}X^{\vartheta} = e^{-i\delta\mathbf{k_j}\cdot\mathbf{x}}\Box X \tag{A5}$$

The conversion between fields, derived by applying the operator $\Box^{\vartheta}$ to the original field X^{ϑ} ($\Box^{\vartheta}X^{\vartheta}$ and $\Box X$) is multiplication with the same conversion factor as when converting between the original rotated and non-rotated fields X^{ϑ} and X.

Proof.

$$\begin{aligned}\nabla X^{\vartheta} &= \\ &= (\nabla X)e^{-i\delta\mathbf{k_j}\cdot\mathbf{x}} + X(-i\delta\mathbf{k}_j)e^{-i\delta\mathbf{k_j}\cdot\mathbf{x}}\end{aligned} \tag{A6}$$

$$\begin{aligned}\nabla^2 X^{\vartheta} &= \\ &= (\nabla^2 X)e^{-i\delta\mathbf{k_j}\cdot\mathbf{x}} + 2(\nabla X)(-i\delta\mathbf{k}_j)e^{-i\delta\mathbf{k_j}\cdot\mathbf{x}} \\ &+ X(-(\delta\mathbf{k}_j)^2)e^{-i\delta\mathbf{k_j}\cdot\mathbf{x}}\end{aligned} \tag{A7}$$

$$(e^{+i\delta\mathbf{k_j}\cdot\mathbf{x}})\Box^\vartheta X^\vartheta = (e^{+i\delta\mathbf{k_j}\cdot\mathbf{x}})\{\nabla^2 X^\vartheta + 2i\mathbf{k}_j(\vartheta)\cdot\nabla X^\vartheta\} \tag{A8}$$

$$= (\nabla^2 X) + 2(\nabla X)(-i\delta\mathbf{k}_j) + X(-(\delta\mathbf{k}_j)^2) \tag{A9}$$

$$+ 2i\mathbf{k}_j(\vartheta)\cdot\nabla X + 2i\mathbf{k}_j(\vartheta)\cdot(-i\delta\mathbf{k}_j)X \tag{A10}$$

$$= (\nabla^2 X) + 2i\mathbf{k}_j(\nabla X) \tag{A11}$$

$$- \cancel{2i\mathbf{k}_j(\vartheta)(\nabla X)} \tag{A12}$$

$$+ X(-\mathbf{k}_j^2 - \mathbf{k}_j(\vartheta)^2 + 2\mathbf{k}_j\cdot\mathbf{k}_j(\vartheta)) \tag{A13}$$

$$+ \cancel{2i\mathbf{k}_j(\vartheta)\cdot(\nabla X)} \tag{A14}$$

$$+ 2i\mathbf{k}_j(\vartheta)\cdot(-i\delta\mathbf{k}_j)X \tag{A15}$$

$$= \Box X \tag{A16}$$

$$+ X\{-\mathbf{k}_j^2 - \mathbf{k}_j(\vartheta)^2 + \cancel{2\mathbf{k}_j\cdot\mathbf{k}_j(\vartheta)} \tag{A17}$$

$$- 2i^2\mathbf{k}_j(\vartheta)^2 + \cancel{2i^2\mathbf{k}_j(\vartheta)\cdot\mathbf{k}_j}\} \tag{A18}$$

$$= \Box X + X\{-\cancel{\mathbf{k}_j^2} + \cancel{\mathbf{k}_j(\vartheta)^2}\} \tag{A19}$$

$$= \Box X \tag{A20}$$

where $\mathbf{k}_j(\vartheta)^2 = \mathbf{k}_j^2$ as rotation preserves distance. □

Lemma 1.2. *From*

$$X^\vartheta(\mathbf{x}) = e^{-i\delta\mathbf{k}_j\cdot\mathbf{x}}X(\mathbf{x}) \tag{A21}$$

it follows

$$(\Box^\vartheta)^n X^\vartheta = e^{-i\delta\mathbf{k_j}\cdot\mathbf{x}}(\Box)^n X \tag{A22}$$

for all positive integers n, $n \in \mathbb{Z}^+$.

The conversion between fields, derived by applying the operator $\Box^\vartheta$ to the original field X^ϑ n times is multiplication with the same conversion factor as when converting between the original rotated and non-rotated fields X and X^ϑ.

Proof. Proof is by induction. Induction base ($n = 1$) is proven in Lemma 1.1. To prove the induction step ($n \to n+1$), we observe that $(\Box^\vartheta)^n X^\vartheta = Y^\vartheta$ is a field in rotated system that corresponds to the field $(\Box)^n X = Y$ in non-rotated system for which equation (A4) holds by induction presumption. Then

$$(\Box^\vartheta)^{(n+1)} X^\vartheta = \Box^\vartheta(\Box^\vartheta)^n X^\vartheta = \tag{A23}$$

$$\Box^\vartheta Y^\vartheta = e^{-i\delta\mathbf{k_j}\cdot\mathbf{x}}\Box Y = \tag{A24}$$

$$e^{-i\delta\mathbf{k_j}\cdot\mathbf{x}}\Box\Box^n X = e^{-i\delta\mathbf{k_j}\cdot\mathbf{x}}\Box^{(n+1)} X \tag{A25}$$

□

Lemma 1.3. *From*

$$X^\vartheta(\mathbf{x}) = e^{-i\delta\mathbf{k}_j\cdot\mathbf{x}}X(\mathbf{x}) \tag{A26}$$

it follows

$$P_n(\Box^\vartheta)X^\vartheta = e^{-i\delta\mathbf{k_j}\cdot\mathbf{x}}P_n(\Box)X \tag{A27}$$

for all positive integers n, $n \in \mathbb{Z}^+$, where

$$P_n(\Box) = \sum_{i=0}^{n} a_i\Box^i \tag{A28}$$

$$P_n(\Box^\vartheta) = \sum_{i=0}^{n} a_i(\Box^\vartheta)^i \tag{A29}$$

is a polynomial function of the operators $\Box$ and $\Box^\vartheta$ of degree n.

Proof.

$$P_n(\Box^\vartheta)X^\vartheta = \sum_{i=0}^{n} a_i(\Box^\vartheta)^i X^\vartheta \tag{A30}$$

$$= \sum_{i=0}^{n} a_i e^{-i\delta\mathbf{k_j}\cdot\mathbf{x}}(\Box)^i X = e^{-i\delta\mathbf{k_j}\cdot\mathbf{x}}P_n(\Box)X \tag{A31}$$

where we used Lemma 1.2 for all powers of the operators. □

Theorem 1.4. *The calculation results obtained in locally rotated system and non-rotated systems are equivalent, meaning that the rotation conversion factor for the complex amplitudes A_j, $e^{-i\delta\mathbf{k_j}\cdot\mathbf{x}}$, converts also the results between both systems.*

Proof. Since the conversion between rotated and non-rotated complex amplitudes is $A^\vartheta(\mathbf{x}) = e^{-i\delta\mathbf{k}_j\cdot\mathbf{x}}A(\mathbf{x})$ it is equivalent to prove that the dynamic equations for the APFC model give equivalent results in both, rotated and non-rotated systems, or

$$\left[\frac{\partial A_j}{\partial t}\right]^\vartheta = \frac{\partial A_j}{\partial t}e^{-i\delta\mathbf{k_j}\cdot\mathbf{x}} \tag{A32}$$

for all $j \in \{1, 2, 3\}$.

We use the following properties of the APFC model:

$$|A_j|^2 = A_j A_j^* \tag{A33}$$

$$\tilde{\mathcal{L}^\vartheta}_j = (1 - \Box^\vartheta)(-r - 3\overline{\psi}^2 - \{\Box^\vartheta\}^2) \tag{A34}$$

$$\mathcal{L}_j^\vartheta = \Box^\vartheta \tag{A35}$$

$$\prod_{k:k\neq j} A_k^* = A_{j+1}^* A_{j-1}^* \tag{A36}$$

$$\mathbf{k}_1 + \mathbf{k}_2 + \mathbf{k}_3 = \mathbf{0} \tag{A37}$$

$$\mathbf{k}_1(\vartheta) + \mathbf{k}_2(\vartheta) + \mathbf{k}_3(\vartheta) = \mathbf{0} \tag{A38}$$

$$e^{+i\delta\mathbf{k_{j+1}}\cdot\mathbf{x}}e^{+i\delta\mathbf{k_{j-1}}\cdot\mathbf{x}} = e^{+i\{\mathbf{k}_{j+1}(\vartheta)+\mathbf{k}_{j-1}(\vartheta)-\mathbf{k}_{j+1}-\mathbf{k}_{j-1}\}\cdot\mathbf{x}}$$

$$= e^{+i\{-\mathbf{k}_j(\vartheta)+\mathbf{k}_j\}\cdot\mathbf{x}}$$

$$= e^{-i\delta\mathbf{k}_j\cdot\mathbf{x}} \tag{A39}$$

$$
\begin{aligned}
A^{\vartheta 2} &= 2\sum_{j=1}^{3} |A_j^{\vartheta}|^2 \\
&= 2\sum_{j=1}^{3} A_j^{\vartheta} A_j^{\vartheta *} \\
&= 2\sum_{j=1}^{3} \cancel{e^{-i\delta \mathbf{k_j}\cdot\mathbf{x}}} A_j \cancel{e^{+i\delta \mathbf{k_j}\cdot\mathbf{x}}} A_j^* \\
&= 2\sum_{j=1}^{3} |A_j|^2 = A^2
\end{aligned}
\tag{A40}
$$

$$
\begin{aligned}
\prod_{k\neq j} A_k^{\vartheta *} &= e^{+i\delta \mathbf{k_{j+1}}\cdot\mathbf{x}} A_{j+1} e^{+i\delta \mathbf{k_{j-1}}\cdot\mathbf{x}} A_{j-1} \\
&= e^{-i\delta \mathbf{k_j}\cdot\mathbf{x}} A_{j+1} A_{j-1}
\end{aligned}
\tag{A41}
$$

It follows

$$
\left[\frac{\partial A_j}{\partial t}\right]^{\vartheta} = \tag{A42}
$$

$$
\begin{aligned}
&= -[\Delta B + B^x \mathcal{L}_j^{\vartheta 2} + 3v(A^{\vartheta 2} - |A_j^{\vartheta}|^2)] A_j^{\vartheta} \\
&+ 2t \prod_{k\neq j} A_k^{\vartheta *}
\end{aligned}
\tag{A43}
$$

$$
\begin{aligned}
&= -e^{-i\delta \mathbf{k_j}\cdot\mathbf{x}} \Delta B A_j \\
&- e^{-i\delta \mathbf{k_j}\cdot\mathbf{x}} B_x \mathcal{L}_j^2 A_j \\
&- e^{-i\delta \mathbf{k_j}\cdot\mathbf{x}} A^2 A_j \\
&- e^{-i\delta \mathbf{k_j}\cdot\mathbf{x}} \cancel{e^{-i\delta \mathbf{k_j}\cdot\mathbf{x}}} A_j \cancel{e^{+i\delta \mathbf{k_j}\cdot\mathbf{x}}} A_j^* A_j \\
&+ e^{-i\delta \mathbf{k_j}\cdot\mathbf{x}} 2t \prod_{k\neq j} A_k^*
\end{aligned}
\tag{A44}
$$

$$
\begin{aligned}
&= e^{-i\delta \mathbf{k_j}\cdot\mathbf{x}} \Big\{ -[\Delta B + B^x \mathcal{L}_j^2 + 3v(A^2 - |A_j|^2)] A_j \\
&+ 2t \prod_{k\neq j} A_k^* \Big\}
\end{aligned}
\tag{A45}
$$

$$
= e^{-i\delta \mathbf{k_j}\cdot\mathbf{x}} \frac{\partial A_j}{\partial t} \tag{A46}
$$

where we used Lemma 1.3 for $\mathcal{L}_j^{\vartheta 2} A_j^{\vartheta}$.

Or for the APFC model published in [5, 6]

$$
\frac{\partial A_j}{\partial t} = \tilde{\mathcal{L}}_j A_j - 3A_j |A_j|^2 - 6A_j \sum_{k:k\neq j} |A_k|^2 - 6\overline{\psi} \prod_{k:k\neq j} A_k^* \tag{A47}
$$

we obtain the same equivalence:

$$
\left[\frac{\partial A_j}{\partial t}\right]^{\vartheta} = \tag{A48}
$$

$$
\begin{aligned}
&= \tilde{\mathcal{L}}^{\vartheta}{}_j A_j^{\vartheta} \\
&- 3A_j^{\vartheta} |A_j^{\vartheta}|^2 - 6A_j^{\vartheta} \sum_{k:k\neq j} |A_k^{\vartheta}|^2 \\
&- 6\overline{\psi} \prod_{k:k\neq j} A_k^{\vartheta *}
\end{aligned}
\tag{A49}
$$

$$
\begin{aligned}
&= e^{-i\delta \mathbf{k_j}\cdot\mathbf{x}} \tilde{\mathcal{L}}_j A_j \\
&- e^{-i\delta \mathbf{k_j}\cdot\mathbf{x}} 3A_j A_j A_j^* \cancel{e^{-i\delta \mathbf{k_j}\cdot\mathbf{x}}} \cancel{e^{+i\delta \mathbf{k_j}\cdot\mathbf{x}}} \\
&- e^{-i\delta \mathbf{k_j}\cdot\mathbf{x}} 6A_j \sum_{k:k\neq j} A_k A_k^* \cancel{e^{-i\delta \mathbf{k_k}\cdot\mathbf{x}}} \cancel{e^{+i\delta \mathbf{k_k}\cdot\mathbf{x}}} \\
&- 6\overline{\psi} A_{j+1}^* e^{+i\delta \mathbf{k_{j+1}}\cdot\mathbf{x}} A_{j-1}^* e^{+i\delta \mathbf{k_{j-1}}\cdot\mathbf{x}}
\end{aligned}
\tag{A50}
$$

$$
\begin{aligned}
&= e^{-i\delta \mathbf{k_j}\cdot\mathbf{x}} \Big\{ \tilde{\mathcal{L}}_j A_j \\
&- 3A_j |A_j|^2 - 6A_j \sum_{k:k\neq j} |A_k|^2 \\
&- 6\overline{\psi} \prod_{k:k\neq j} A_k^* \Big\}
\end{aligned}
\tag{A51}
$$

$$
= e^{-i\delta \mathbf{k_j}\cdot\mathbf{x}} \frac{\partial A_j}{\partial t} \tag{A52}
$$

where we used Lemma 1.3 for $\tilde{\mathcal{L}}^{\vartheta}{}_j A_j^{\vartheta}$ □

[1] K. R. Elder, M. Katakowski, M. Haataja, and M. Grant, Phys. Rev. Lett. **88**, 245701 (2002).

[2] K. R. Elder and M. Grant, Phys. Rev. E **70**, 051605 (2004).

[3] N. Goldenfeld, B. P. Athreya, and J. A. Dantzig, Phys. Rev. E **72**, 020601 (2005).

[4] N. Goldenfeld, B. P. Athreya, and J. A. Dantzig, J. Stat. Phys. **125**, 1019 (2006).

[5] B. P. Athreya, N. Goldenfeld, J. A. Dantzig, M. Greenwood, and N. Provatas, Phys. Rev. E **76**, 056706 (2007).

[6] M. Berčič and G. Kugler, Phys. Rev. E **98**, 033303 (2018).

[7] N. Faghihi, N. Provatas, K. R. Elder, M. Grant, and M. Karttunen, Phys. Rev. E **88**, 032407 (2013).

[8] M. Seymour, F. Sanches, K. Elder, and N. Provatas, Phys. Rev. B **92**, 184109 (2015).

[9] V. Heinonen, C. V. Achim, J. M. Kosterlitz, S.-C. Ying, J. Lowengrub, and T. Ala-Nissila, Phys. Rev. Lett. **116**, 024303 (2016).

[10] B. P. Athreya, N. Goldenfeld, and J. A. Dantzig, Phys. Rev. E **74**, 011601 (2006).

[11] M. Greenwood, N. Provatas, and J. Rottler, Phys. Rev. Lett. **105**, 045702 (2010).

[12] M. Greenwood, N. Ofori-Opoku, J. Rottler, and N. Provatas, Phys. Rev. B **84**, 064104 (2011).

[13] N. Ofori-Opoku, J. Stolle, Z.-F. Huang, and N. Provatas, Phys. Rev. B **88**, 104106 (2013).

[14] P. Hirvonen, M. M. Ervasti, Z. Fan, M. Jalalvand, M. Seymour, S. M. Vaez Allaei, N. Provatas, A. Harju, K. R. Elder, and T. Ala-Nissila, Phys. Rev. B **94**, 035414 (2016).

[15] M. Salvalaglio, R. Backofen, A. Voigt, and K. R. Elder, Phys. Rev. E **96**, 023301 (2017).

[16] K.-A. Wu, A. Adland, and A. Karma, Phys. Rev. E **81**, 061601 (2010).

[17] G. Kocher and N. Provatas, Phys. Rev. Lett. **114**, 155501 (2015).

[18] M. Seymour and N. Provatas, Phys. Rev. B **93**, 035447 (2016).

[19] K. R. Elder, Z. Chen, K. Elder, P. Hirvonen, S. Mkhonta, S.-C. Ying, E. Granato, Z.-F. Huang, and T. Ala-Nissila, J. Chem. Phys. **144**, 174703 (2016).

[20] K. R. Elder, Z.-F. Huang, and N. Provatas, Phys. Rev. E **81**, 011602 (2010).

[21] K. R. Elder and Z.-F. Huang, J. Phys.: Condens. Matter **22**, 364103 (2010).

[22] R. Prieler, J. Hubert, D. Li, B. Verleye, R. Haberkern, and H. Emmerich, J. Phys.: Condens. Matter **21**, 464110 (2009).

[23] R. Wittkowski, H. Löwen, and H. R. Brand, Phys. Rev. E **82**, 031708 (2010).

[24] R. Wittkowski, H. Löwen, and H. R. Brand, Phys. Rev. E **83**, 061706 (2011).

[25] Z.-F. Huang, K. R. Elder, and N. Provatas, Phys. Rev. E **82**, 021605 (2010).

[26] R. Spatschek and A. Karma, Phys. Rev. B **81**, 214201 (2010).

[27] N. Ofori-Opoku, V. Fallah, M. Greenwood, S. Esmaeili, and N. Provatas, Phys. Rev. B **87**, 134105 (2013).

[28] V. Heinonen, C. V. Achim, K. R. Elder, S. Buyukdagli, and T. Ala-Nissila, Phys. Rev. E **89**, 032411 (2014).

[29] M. Salvalaglio, R. Backofen, K. R. Elder, and A. Voigt, Phys. Rev. Materials **2**, 053804 (2018).

[30] O. V. Yazyev and S. G. Louie, Phys. Rev. B **81**, 195420 (2010).

[31] M. Greenwood, J. J. Hoyt, and N. Provatas, Acta Mater. **57**, 2613 (2009).

[32] M. Greenwood, *Using Phase-Field Modeling With Adaptive Mesh Refinement To Study Elasto-Plastic Effects In Phase Transformations*, Ph.D. thesis, McMaster University (2008).